



HAL
open science

Experimental Study of Flow Control on Bluff Body using Piezoelectric Actuators

Nabil Tounsi, Rafika Mestiri, Laurent Keirsbulck, Hamid Oualli, Samir
Hanchi, Fethi Aloui

► **To cite this version:**

Nabil Tounsi, Rafika Mestiri, Laurent Keirsbulck, Hamid Oualli, Samir Hanchi, et al.. Experimental Study of Flow Control on Bluff Body using Piezoelectric Actuators. *Journal of Applied Fluid Mechanics*, 2016, 9 (2), pp.827-838. 10.18869/acadpub.jafm.68.225.24488 . hal-03448166

HAL Id: hal-03448166

<https://uphf.hal.science/hal-03448166v1>

Submitted on 14 Apr 2022

HAL is a multi-disciplinary open access archive for the deposit and dissemination of scientific research documents, whether they are published or not. The documents may come from teaching and research institutions in France or abroad, or from public or private research centers.

L'archive ouverte pluridisciplinaire **HAL**, est destinée au dépôt et à la diffusion de documents scientifiques de niveau recherche, publiés ou non, émanant des établissements d'enseignement et de recherche français ou étrangers, des laboratoires publics ou privés.



Distributed under a Creative Commons Attribution - NonCommercial - ShareAlike 4.0 International License



Experimental Study of Flow Control on Bluff Body using Piezoelectric Actuators

N. Tounsi², R. Mestiri³, L. Keirsbulck¹, H. Oualli², S. Hanchi², and F. Aloui^{1†}

¹ LAMIH CNRS UMR 8201, F-59313 Valenciennes, France

² Laboratory of Fluid Mechanics, EMP, Bordj El Bahri, 16046 Algiers, Algeria

³ Laboratoire d'Etude des Systèmes Thermiques et Énergétiques, ENIM, Avenue Ibn El Jazzar 5019 Monastir, Tunisie

† Corresponding Author Email: fethi.aloui@univ-valenciennes.fr

(Received January 11, 2015; accepted March 28, 2015)

ABSTRACT

Active flow control is experimentally investigated on a car-type bluff body. The actuation is based on a synthetic jet actuator placed at the top of the Ahmed body rear window. In the present paper, a synthetic jet characterization is presented, the frequencies and the optimal amplitudes with regard to the spatial evolution are analyzed. All the measurements are carried out in a wind tunnel at Reynolds numbers based on the body length between 10^6 and 3×10^6 . The bluff body shows a maximum drag reduction of 10% when optimal control is applied. Independent effect of the reduced frequency and the momentum coefficient actuation parameters on the drag reduction are also detailed in the present paper. This reduction induces changes in the flow field due to the piezoelectric actuation. The flow topology modification is investigated via particle image velocimetry measurements in order to estimate the flow response to a local excitation and to understand the mechanism involved in the aerodynamic drag control.

Keywords: Flow control; Drag reduction; Synthetic jet; Bluff body; Piezoelectric actuator.

NOMENCLATURE

C_D	drag coefficient	U_∞	upstream velocity
C_μ	momentum coefficient	U_{cl}	centerline actuator velocity
$C_{\mu lim}$	critical momentum coefficient	U_{max}	maximum blowing velocity
d	slit spacing	\bar{U}_{cl}	phase average centerline actuator velocity
F^+	reduced frequency	\tilde{U}_j	mean spatial actuator blowing velocity
f_j	actuator frequency	W	ahmed body width
H	ahmed body height	x	upstream direction
I_j	actuator injected momentum	y	vertical direction
L	ahmed body length		
N	numbers of duty cycle	ϵ_n	uncertainty on the velocity average
n	numbers of PIV instantaneous fields	ΔC_D	drag variation
Re_L	ahmed body Reynolds number	F_D	drag force
S_j	slot actuator section	σ	velocity standard deviation
S_{front}	frontal surface of the Ahmed body	Φ	angular phase of the synthetic jet
U_e	actuator supply voltage		
\bar{U}_j	actuator mean temporal blowing velocity		

1. INTRODUCTION

The need to reduce the energy consumption through drag reduction leads to focus investi-

gations on active flow control as an interesting alternative to passive solutions Kourta and Gilliéron (2009). However, significant progresses are necessary to overcome barriers as

3D flow complexity and unsteadiness associated with it. Many studies are devoted to analyze the flow around simplified car geometry Ahmed, *et al.* (1984) and to investigate the unsteady mechanisms of the bubble separation that develop themselves on the rear slanted surface of the Ahmed model with a slant angle of 25° . Thacker (2010) and Thacker *et al.* (2010) showed that the physical effect of the low frequency unsteadiness of the shear layer flow is linked to the mechanism of separation as previously shown in the literature Krajinovic and Davidson (2005), Hinterberger *et al.* (2003). However, some new unanswered questions are reported in the literature and highlight that all the physical mechanisms responsible of the overall flapping are still unknown whereas they represent a significant interest in sight of flow control applications. In parallel, research works are in progress to find control solutions able to suppress or to reduce the separated bubble size on a bluff body. Today, European policy impose more and more strict rules concerning the design of “clean” automotive, so that the efforts of the car manufacturers are directed to find a way to increase the performance of a given system in order to reduce the gas emissions responsible for the greenhouse effect. The engineers have to consider innovative solutions based on flow control, particularly for flow separation which generally has deleterious effects on aerodynamic performance. Indeed, the separation phenomena, inherent to the bluff bodies, is at the origin of the drag increase and consequently of the fuel consumption. Both active and passive methods of flow control can be applied to avoid or reduce this type of separation-induced performance loss. The passive control systems consist on the use of discrete obstacles, added around or on the roof of the vehicle. Various passive means for flow control are well investigated. A lot of successful studies are done using passive strategies such as splitter plates at the rear blunt end Gilliéron and Kourta (2010), porous layers on the different model surfaces (Bruneau *et al.* (2007), Bruneau and Mortazavi (2008)) or vortex generators on the vehicle rear window (Beaudoin and Aider (2008), Aider *et al.* (2010)). Fourrié *et al.* (2011) obtained 9% of drag reduction using a classical automotive style deflector placed on the upper edge of a 25° car model. An approach using vortex generators to produce coherent streaks that increase or decrease the separated bubble were also carried out by Pujals *et al.* (2010) leading to 10% drag reduction when the roughness array is optimally placed on the roof of the bluff body. However, conventional passive control

techniques consisting in modifying the shape of the vehicle to reduce the aerodynamic drag are not sufficient Leclerc *et al.* (2006a). The active flow control may offer more creative possibilities to the automobile designers because it can ensure the control without additive sharp appendix or strong geometrical modification. Current research projects are now focusing on active flow control techniques performed by using actuators that require a power generally taken on the principal generator of energy of the vehicle Kourta and Gilliéron (2009). Their use requires mechanical, electromagnetic, electric, piezoelectric or acoustic systems placed in the hollow parts of the vehicle. Their weights and their overall dimensions must be miniaturized to reduce their impacts on consumption and requested volume. Modi(1997) has experimentally investigated the moving surface boundary layer control (MSBC) provided by rotating cylinders located at the flow separation area. In his review, the author has shown the effectiveness of the used actuator for several studied aerodynamic geometries. Another kind of actuators is based on the surface plasma created by an electrical discharge. These actuators are largely studied for aeronautical applications and a little studied for automotive applications. The experimental study done by Boucinha (2009) showed that the plasma control application on the Ahmed body did not lead to significant drag reductions. However, fluid actuators have interesting applications in the automotive area. The first advantage of these actuators is that they are easily embedded and not visible by the user. The adopted techniques consist on suction or blowing through circular or rectangular slots. The suction and blowing can be continuous or intermittent (Gilliéron *et al.* (2013)). Joseph *et al.* (2011) have used pulsed jets for flow control on an Ahmed model with 25° slant angle, they have tested four distinct configurations of flow control: rectangular pulsed jets aligned with the spanwise direction or in winglets configuration on the roof end and rectangular jets or a large open slot at the top of the rear slant. The authors showed that depending on the used configuration the jet velocity or the pulsation frequency or the both are key parameters to optimize the drag reduction, for all studied cases the maximum drag reductions obtained are between 6 and 8%. Other studies done on the continuous suction or blowing are shown to be effective for the drag reduction (Rouméas *et al.* (2005), Rouméas *et al.* (2006), Rouméas *et al.* (2009)). Experimental studies of Lehugeur *et al.* (2010) showed that the control using the steady suction or blowing normal to the lateral

face of the Ahmed body change significantly the topology of the vortex core and reduce the drag. Aubrun *et al.* (2011) have applied an actuation consisting on steady micro-jet array placed 6mm downstream of the separation line between the roof and the slanted rear window. This actuation has reduced the drag coefficient by 9 to 14 % and the lift coefficient up to 42%. Alternating suction-blowing mechanism or synthetic jet are efficient methods for control because they improve the aerodynamic performances. Several synthetic jet actuators are designed, they can be grouped into three categories: the piezoelectric devices (Smith and Glezer (2002), Schaffler *et al.* (2002)), mechanical devices (Rediniotis *et al.* (1999), Crittenden and Glezer (2006), Joseph *et al.* (2013)) and the acoustic devices (Erk (1997), McCormick (2000), Tesar and Kordik (2010)). A constraint of the piezoelectric actuators is that the output velocity depends on the resonance frequency contrary to the mechanical actuators where the expulsion speed increases linearly with the frequency. However, a piezoelectric device has several advantages, it is easier to implement and it requires only a few energetic power to operate. Many studies are done with this type of actuation on different configurations (Jenkins *et al.* (2002), Chen *et al.* (2000)). Leclerc *et al.* (2006a) and Leclerc *et al.* (2006b) have numerically examined the active synthetic jet control around a simplified car model and he showed that a significant mean aerodynamic drag reduction of about 30% can be obtained with the optimum configuration. The aim of the present work is to study experimentally the effect of synthetic jets on the flow above a simplified car geometry. We will present a detailed characterization of the synthetic jet created by the piezoelectric actuator. Then we will focus on the application of the aerodynamic control on the rear window of the studied model. So, we will show the effect of the actuator on drag reduction and then we will detail the modifications on the topology flow around the Ahmed body.

2. EXPERIMENTAL SETUP

2.1 Facilities, Model and Flow Conditions

All the measurements are carried out in a closed-circuit subsonic wind tunnel of the LAMIH which has a 6m long close test section with a square cross-section $2 \times 2m^2$ Fig. 1. The maximum free-stream velocity is 60m/s.

The blockage ratio is evaluated to 3% and the measured turbulence intensity of the upstream flow is 0.7%. The free-stream velocity U_∞ is

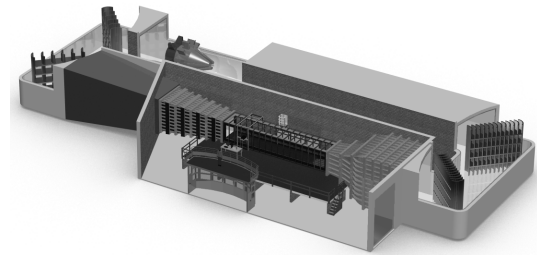


Fig. 1. Closed-circuit subsonic wind tunnel.

measured by hot-wire anemometry. The bluff-body used in our study is full-scale Ahmed body with a 25° rear slant angle classically used in numerous studies. The model is 1.044m long, 0.389m wide, 0.288m high and the rear window is 0.222m long Fig. 2.

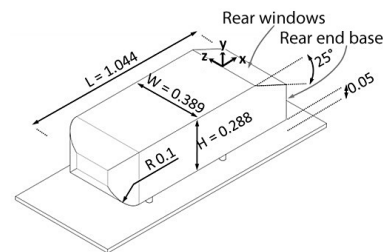


Fig. 2. Geometry of the Ahmed car model (dimensions in m).

The model is placed at the center of the wind tunnel section at a height of 50mm on a profiled plate. The model is mounted over a raised floor in order to limit the boundary layer thickness and minimize the upstream perturbations Fig. 3.

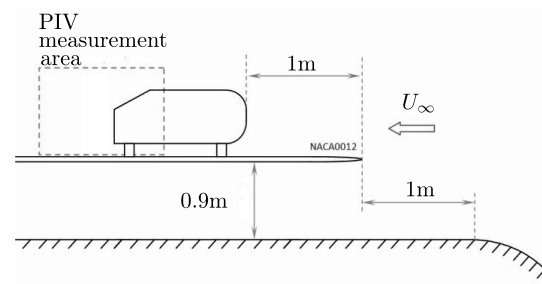


Fig. 3. Ahmed body location in the test section.

The sub-floor is optimized in order to improve the under-floor flow circulation and its dimensions are chosen large enough to avoid the flow perturbations. This placement of the Ahmed body allows us to preview a large clearance behind the model in order to realize a wake exploration.

2.2 Equipment and Methods

Drag balance measurements

The time-averaged drag F_D values were measured with an external six-component aerodynamic balance. The drag coefficient is defined as follows:

$$C_D = \frac{F_D}{\frac{1}{2}\rho U_\infty^2 S_{front}} \quad (1)$$

where S_{front} is the projected frontal area of the model and ρ the density. The absolute uncertainty on the drag coefficient depends on both the tolerance of the load cell provided by the manufacturer and on the quality of the support. The sensor tolerance is relatively negligible. The mass weighing is highly dependent on the support stability. The typical global error on the measurement of the drag forces is less than 3%.

Hot Wire Anemometry measurements

Synthetic jet velocity measurements are done by hot wire anemometry, the probe support is fixed to a vertical displacement system. The acquisition and processing system is a standard one component boundary-layer hot-wire probe (DANTEC Streamline software). The used probe is DANTEC 55P15 that has a wire diameter of $5\mu m$ and a wire length of $1mm$. The single wire probe is moved using a motorized device. Each velocity signals consist of 300s long signal samples at $1kHz$.

Particle image velocimetry measurements

Velocity field identification was done using standard particle image velocimetry for the two dimensional two components (2D-2C) measurements. PIV measurements planes are indicated on Fig. 3. Velocity measurements were taken in the longitudinal model symmetry plane (xy-plane). The used system is a TSI set with the processing software INSIGHT 3G. Light sheets are provided by a double-pulsed ND-YAG laser operating at $532nm$, with a $7.25Hz$ frequency. The maximum energy of each pulse is $200mJ$ for $8ns$. The delay between the two pulses is fixed so that particles move from about a fourth of the interrogation window during this delay. The laser sheet is generated by placing a semi-cylindrical diverging lens at the exit of the laser beam in order to allow the opening of the laser sheet. The measured field sizes, the corresponding details of the interrogation window and the spatial resolution are indicated in Table 1 for each studied case.

Table 1 PIV measurement conditions (SF: small field and LF: large fields)

	PIV (SF)	PIV (LF)
Real field size (mm^2)	6×6	335×335
Sensor size (px^2)	2048×2048	2048×2048
Integration box (px)	16×16	24×24
Spatial resolution (mm)	0.05	3.9

A 50% overlap rate has been applied to reduce the velocity grid spacing. The time averaged fields are obtained from 1500 instantaneous fields. The flow seeding is made by olive oil using a fog generator; the particles mean diameter is about $2.5 \times 10^{-6}m$. Which represents approximately 2 pixels in agreement with the recommendations given by Prasad *et al.* Prasad *et al.* (1992). The resulting bias error on the particle is about 0.2 pixels. So, when normalizing with the mean displacement of the particles in the free stream, it leads to a relative error on velocity of about 3%. A statistical error is also calculated on the averaged velocity and we have used the central limit theorem. For n PIV image pairs and for confidence interval of 95%, the uncertainty on the velocity average is $\epsilon_n = 1.96 \times \frac{\sigma}{\sqrt{n}}$, where σ is the velocity standard deviation. In our case, with $n = 1500$, the statistical error is less than $10^{-2} \times U_\infty$ in the external flow velocity and up to $3.4 \times 10^{-2} \times U_\infty$ in the wake flow.

2.3 Actuator Design and Location

Flow control is effected thanks to an in-house made piezoelectric actuators creating a pulsed jet. The actuator is based on an oscillating cavity volume resulting on twelve KPSG100 piezoelectric membranes covering its internal wall Fig. 4. The synthetic jet actuator has $234mm$ as length, $16mm$ as wide and $40mm$ as height and it can be considered as a compacted actuator. The real actuator is also shown in Fig. 4.

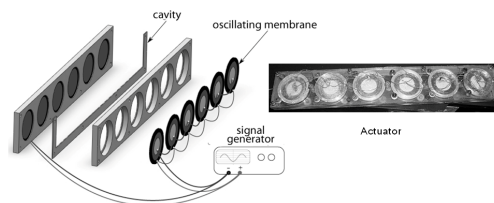


Fig. 4. Piezoelectric actuator.

A synthetic jet actuator is mounted on the studied Ahmed body and placed just before the edge between the end of the roof and the top of the rear window Fig. 5. Main dimensions of the actuator output slot are a width (d) of $1mm$ and a

length (W) of 389mm (showed in Fig. 5). All the connections pass through one Ahmed body foot and the piezoelectric membranes are supplied by an electronic system composed of a generator function and a power amplifier.

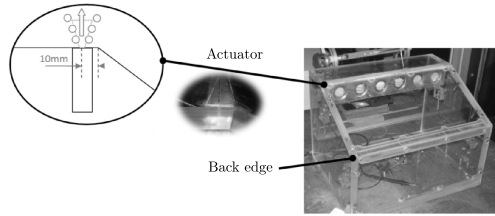


Fig. 5. Actuators location on the Ahmed body.

3. RESULTS AND DISCUSSION

3.1 Actuator Performance

Before flow control experiments, this section aims to characterize the actuator behavior in terms of space and time average behaviors and also provided their main dynamical parameters.

Output time-average slot velocity

The output velocity induced through the actuator slot varies with the synthetic jet actuator frequency f_j and the supply voltage U_e . For the present actuator, we note a main resonance peak at a frequency of 325Hz and a secondary one at 425Hz . A dynamic characterization is done for these two resonance frequencies and for a supply voltage range of 2.0V to 8.6V before amplification. We observe that the average jet velocity at the slot output increases linearly with the excitation voltage and that the deformation of the piezoelectric membranes is proportional to the applied voltage. So, for a given frequency, we can increase the velocity amplitude by increasing the supply voltage. The output slot velocity has a quasi-periodic evolution, consequently in order to study the operating cycle, we have performed a phase average for several excitation signal amplitudes (example provided in Fig. 6). The phase-averaged velocity on N periods is written as follows:

$$\tilde{U}_{cl} = \frac{1}{N} \sum_{i=1}^N U_{cl}(t + iT) \quad t \in [0, T] \quad (2)$$

The synchronization is done by simultaneous recording of the sinusoidal signal of the actuators excitation before amplification and of the velocity signal obtained by hot wire anemometry. These phase averages highlight the blowing and the suction phases. Except the directional insensitivity of the hot wire, there is a slight

phase shift of the measured flow velocity relative to the excitation signal. The in-house made actuator can reach a maximum velocity of 8m/s for a supply voltage of 8.6V Fig. 6.

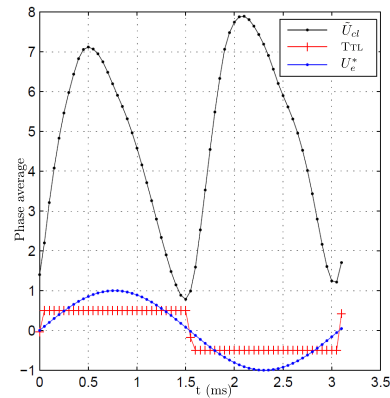


Fig. 6. Example of phase-averaged velocity \tilde{U}_{cl} of the synthetic jet at the center of the slot for a supply voltage of $U_e = 8.6\text{V}$ and at 325Hz . * symbol denotes the normalized values.

Spatial behavior of the induced flow

Spatial distribution of the flow induced by the actuator has been also studied using small fields PIV measurements as previously described. The particle image velocimetry phase synchronization is achieved by using a TTL master signal following the procedure described in Fig. 7. The rising front of the TTL signal is used as a reference to synchronize both the actuator and the PIV measurements. The induced flow topology obtained for the maximum suction phase is plotted in Fig. 8 and shows the development of two vortices at the vicinity of the slot and the existence of a lowest saddle point that defines the near-wake and the far-wake flow region. The same flow topology has already been shown by Smith *et al.* Smith and Glezer (2002) and Schaffler *et al.* Schaffler *et al.* (2002). In the synthetic jet flow, we can identify a near-field and a far-field regions delimited by the red line in Fig. 8.

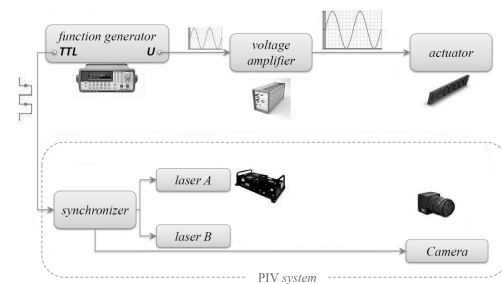


Fig. 7. Synchronization principle of the PIV using a TTL trigger signal.

We can show that during the blowing phase the stagnation point is relatively close to the slot output and it moves away during the suction phase. The synthetic jet presented here is slightly inclined, and is not perfectly symmetric as it was also observed in the study of Smith *et al.* Smith and Glezer (2002). This asymmetrical behavior is probably due to the slot design.

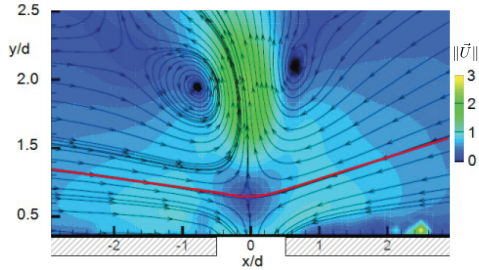


Fig. 8. Velocity magnitude field at the maximum suction phase for $U_e = 4.0V$ and $f = 325Hz$.

In order to describe the induced flow dynamical behavior and especially the injected momentum mechanism, we compute the averaged flow topology for twenty angular phases for a duty cycle ($\Phi = 0^\circ$ to 360°) as shown in Fig. 9. We note that the flow generated by the actuator is a typical synthetic jet flow as previously described by Kotapati *et al.* Kotapati and Mittal (2005) and consists of two counter-rotating vortices. The experimental vorticity distribution shows that the formation of a pair of vortices is due to the detachment and the rolling of the fluid through the slot output when the angular phase of the synthetic jet Φ is between $\Phi = 133^\circ$ and $\Phi = 190^\circ$. These vortices grow and then they shed around $\Phi = 38^\circ$ during a duty cycle.

Actuator dynamical parameters

In order to obtain the mean actuator momentum, we need to evaluate the averaged temporal velocity during the blowing phase. Since the hot wire anemometry sensor is not sensitive to flow direction, the velocity measurements of the successive blowing and suction are biased. Both used measurement techniques give similar temporal evolution with nearly the same phase duration. But, in the region near to the slot, PIV measurements suffer of a lack of accuracy due to the wall reflections. For that reason, we use the hot wire anemometry velocity measurements as reference for the momentum coefficient computation. The synoptic of hot wire signal processing adopted for momentum computation is reported on Fig. 10. Near-field measurements are made phase-locked to the driv-

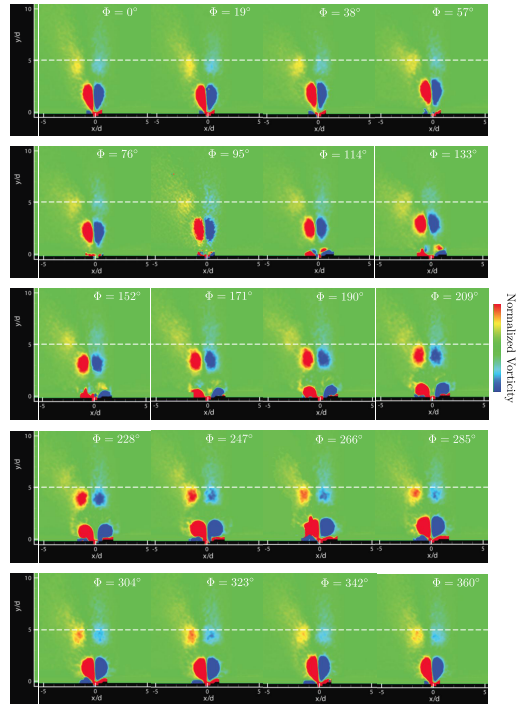


Fig. 9. Phase by phase spatio-temporal normalized vorticity distribution of the synthetic jet ($\Phi = [0^\circ, 360^\circ]$) for a frequency of 325 Hz and a supply voltage of 3V.

ing waveform, and are phase averaged over a cycle. Since the centerline velocity follows a sinusoidal law, the maximum blowing velocity U_{max} is deduced and corrected using the Stokes number in order to evaluate the blowing average spatial velocity \tilde{U}_j of the synthetic jet.

The velocity correction was necessary since the velocity profile at the exit of the slot varies with

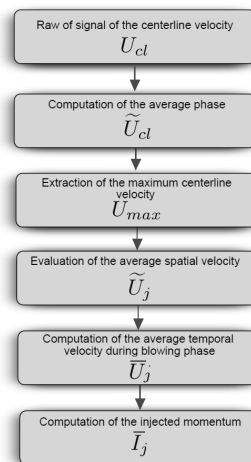


Fig. 10. Synoptic of hot wire signal processing adopted for momentum computation.

Table 2 Actuator characteristics for $f_j = 325Hz$ against U_e

U_e (V)	U_{max} (m/s)	\bar{U}_j (m/s)	\bar{I}_j (kg.m/s ²)
2.00	0.83	0.70	0.1×10^{-3}
3.00	2.41	2.05	0.9×10^{-3}
4.00	4.18	3.56	2.6×10^{-3}
5.00	6.37	5.41	6.1×10^{-3}
6.00	7.89	6.71	9.3×10^{-3}
7.00	8.84	7.52	11.7×10^{-3}
8.00	9.25	7.86	12.8×10^{-3}
8.60	9.76	8.30	14.2×10^{-3}

the Stokes number and depends on it, the profile may change from parabolic to constant. The obtained averaged spatial velocity of blowing is used to calculate the averaged temporal velocity during blowing phase \bar{U}_j and then to compute the actuator injected momentum \bar{I}_j . All parameters relating to the present in-house made actuator are reported in Table 2 for the first resonating mode ($f_j = 325Hz$).

3.2 Flow Control

The actuator described before is now used in order to control the flow involved at the rear back of the Ahmed body. In this section, after a brief definition of the reduced control parameters used here and including both actuator and external flow characteristics, we investigate the drag reduction performance and the global flow behavior.

Control parameters

The effect of the synthetic jet actuator on the external flow involving around the Ahmed body is investigated. All the following experiments are carried out in the closed-circuit subsonic wind tunnel on a full-scale Ahmed model as described previously. The upstream flow velocities used here are in the range of $16m/s$ to $45m/s$. We will present the efficiency of the aerodynamic control, using the momentum coefficient and the reduced frequency parameter. The momentum coefficient C_μ is written as follows:

$$C_\mu = \frac{S_j}{S_{front}} \left(\frac{\bar{U}_j}{U_\infty} \right)^2 = \frac{d}{H} \left(\frac{\bar{U}_j}{U_\infty} \right)^2$$

With \bar{U}_j the average jet velocity, U_∞ the infinite upstream velocity, S_j the jet exit section, S_{front} the cross-section area of the studied model, H the model height and d the slot width. The reduced frequency is defined by:

$$F^+ = \frac{f_j H}{U_\infty}$$

Where f_j is the excitation frequency of the piezoelectric membranes. As the model weight is constant, the reduced frequency is mainly depending on the excitation frequency or the flow velocity.

Aims of the active flow control

Several studies deal with the active flow control and aim to reduce separation occurring on a 3D bluff body. But, only few of them focus on the choice of the control parameters that contribute to improve the aerodynamic performance Joseph *et al.* (2013), Gilliéron *et al.* (2013). However, there are two main parameters described in the literature; the forcing reduced frequencies and the momentum coefficient relating to the velocity amplitude of the synthetic jet. These parameters can be involved independently and constitute two different ways for controlling the flow. Up to now, there is no consensus for selecting optimized frequencies or momentum coefficient for a given Reynolds number. In the present study, a comparison between the two parameters will be done by using the synthetic jets in the reduced frequencies range of 2.08 up 7.65 for various Reynolds numbers from 10^6 and 3×10^6 and also for different momentum coefficients up to 10^{-3} . Several publications have shown the efficiency of the synthetic jets to suppress the separation on various configurations. Nevertheless, the physical comprehension and the choice of the control parameters are not sufficiently developed. This may be due to the multiplicity of the parameters that can have potential self-interactions, for example: the frequency, the amplitude, the forcing spatial distribution and the forcing temporal distribution, the orifice form, the angle of attack, the actuator position, the actuators interactions, the Reynolds number, and so forth... Three of these parameters will be studied in this paper, the frequency, the forcing amplitude and the Reynolds number.

Drag reduction

Maximum drag reduction against various Reynolds number Re_L between 10^6 and 3×10^6 are depicted in Fig. 11. We note that the drag reductions are more significant and reach a maximum drag reduction of 10% for $Re_L = 2.3 \times 10^6$.

A same configuration is studied by Leclerc Leclerc (2008), Leclerc *et al.* (2006b) and sim-

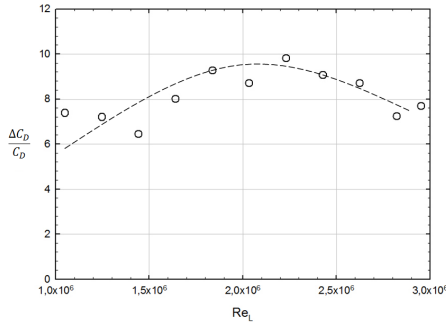


Fig. 11. Drag reduction against Re_L .

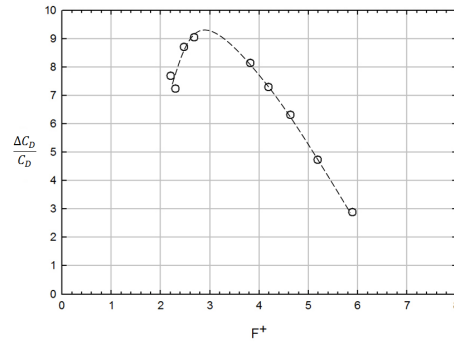


Fig. 12. Drag reduction against F^+ for $C_\mu \propto 2.5 \times 10^{-4}$.

ilar drag reductions are observed. The explanation of the drag reduction mechanism is detailed by Joseph Joseph (2012) and it is associated with momentum injection ensured by created structures at a frequency close to the Kelvin-Helmholtz frequency. These induced structures create a mixing between the low-velocity separated region and the high-velocity external flow and then decrease the separation region. An interesting parameter for the control is the duty cycle duration of the periodic perturbation. Duriez *et al.* Duriez *et al.* (2011) showed that the efficiency of the control depends on the synchronization between the natural emission of the vortices and the forced emission by the control system. The control is optimum when the frequency of the forced vortices emission is close to the natural frequency Ho and Huang (1982). In order to dissociate the parameter effect, drag measurements for the same momentum coefficient $C_\mu \propto 2.5 \times 10^{-4}$ are analyzed and plotted in Fig. 12. Measurements show that the higher drag reductions are obtained with reduced frequencies range between 2.5 and 3, beyond this magnitude the drag reductions drop strongly Fig. 12. It seems that the reduced frequency is an important parameter to control the flow separation, since the drag reduction mechanism through separation control over the rear window of a bluff body is closely related to the Kelvin-Helmholtz frequency Joseph (2012) , Duriez *et al.* (2011). The Kelvin-Helmholtz frequency associated with shear layer that develops itself on the rear window of Ahmed body couldn't be identified in this work, however, in literature Thacker (2010), Thacker *et al.* (2010), Joseph (2012) , Joseph *et al.* (2013) this frequency is corresponding to Strouhal number F^+ of about 1.15 up 3.66 which is near to the reduced frequency corresponding to the maximum drag reduction found in the present study.

Fig. 13 illustrates the drag reductions measured for several momentum coefficient values. The

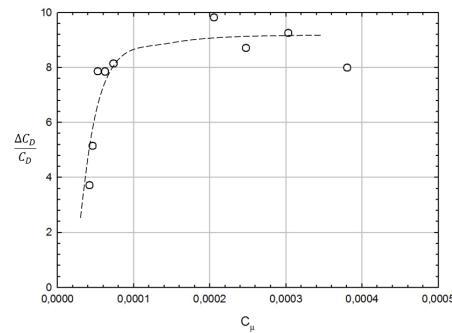


Fig. 13. Drag reduction against C_μ for $F^+ \propto 3.5$.

maximum drag reduction close to 10% is obtained for a momentum coefficient of $C_{\mu lim} = 2 \times 10^{-4}$, this reduction seems to remain constant for higher momentum coefficient values. The momentum coefficient is a significant parameter, but from a certain value (around $C_{\mu lim}$), its effect seems to be optimal. So in order to better understand the physical mechanism at the origin of the drag reduction, we will study the flow topology for two different reduced frequencies (case1: $F^+ = 5.85$ and case2: $F^+ = 7.65$) and for $C_\mu > C_{\mu lim}$. Actuator parameters and drag reduction associated to the large fields PIV measurements employed to estimated the flow topology at $Re_L \propto 10^6$ are reported in Table 3.

Topology of the controlled flow

Table 3 Actuator parameters and drag reduction at $Re_L \propto 10^6$ for large fields PIV measurements

f_j (Hz)	325	425
F^+	5.85	7.65
\bar{U}_j (m/s)	8.30	4.54
$C_\mu (\times 10^4)$	9.34	2.79
$\Delta C_D/C_D$ (%)	7.4	1.9

In this paragraph we will explain the mechanisms that lead to the obtained drag reductions, the control effects are deduced from the changes in the average topology of the flow over the rear end window and in the near wake. The control effect of actuator is mainly concentrated on the separated bubble on the rear window of the Ahmed body. Standard PIV measurements were taken in the longitudinal symmetry plane for the reference case: without control Fig. 14.

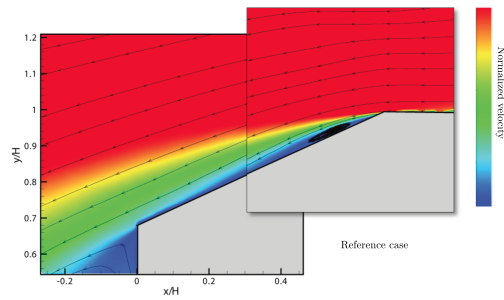


Fig. 14. Flow topology (reference case).

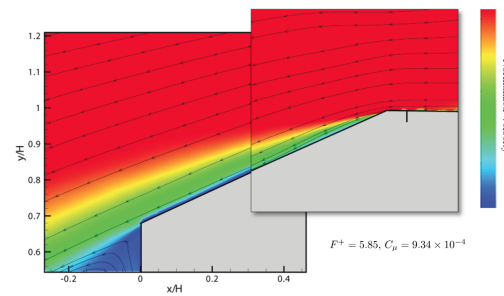


Fig. 15. Topology of the controlled flow (case1): $F^+ = 5.85, C_\mu = 9.34 \times 10^{-4}$.

We note that the separated bubble is removed completely in the case1 Fig. 15, the drag reduction in this case is of 7.4%. In case2 Fig. 16, for a higher reduced frequency, the streamlines are deflected towards the model surface and the attachment node moves upward of the window. We note a decrease of separated bubble size (around 25%) that may be a result of a smaller vorticity at the first part of the rear window leading to a drag reduction of about 1.9%. Figure 14, 15 and 16 also show the velocity topology at the end of the rear window, before and after actuation. We observe a reduction of the boundary layer thickness for the controlled cases. Also, the reduction of the boundary layer thickness is accompanied by an increase of the velocity near the wall. Similar results are obtained by Leclerc Leclerc (2008). The injected momentum allows the flow to resist to the adverse pressure gradient.

In the following, we will present the vorticity

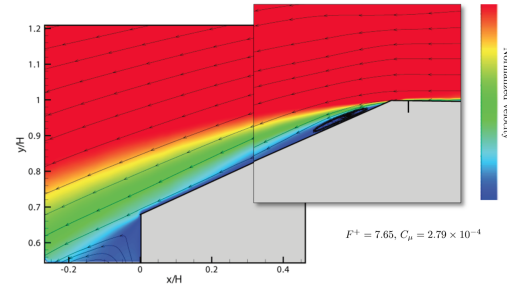


Fig. 16. Topology of the controlled flow (case2): $F^+ = 7.65, C_\mu = 2.79 \times 10^{-4}$.

cartography analysis for the reference and the controlled flow (only case1) in order to increase our physical comprehension through the main modification of the base flow topology. Vorticity maps are based on the velocity fields and they contain the average flow streamlines Fig. 17. Without control Fig. 17(left), streamlines show a recirculation region associated with the separated bubble classically observed at the rear window of an Ahmed body. The upper limit of the separated bubble is associated with the development of a strong spanwise vorticity sheet. The vorticity sheet reflects the development of a shear layer resulting of the boundary layer separation at the end of the roof with a relative angle of almost 13° . At the wall, the flow recirculation directed upward of the rear window forms a vorticity sheet with very low values, even negative. The vorticity distribution in the controlled case is presented for the highest momentum coefficient $C_\mu = 9.34 \times 10^{-4}$ Fig. 17 (right), the vorticity sheet is almost tangent to the rear window surface and the separated bubble disappears. When the momentum coefficient increases, the flow is reattached to the model surface and the shear layer is directed tangentially to the window. Indeed, the control effect on the reduction of the separated bubble size depends on the shear layer direction. Physically, the synthetic jet action on the separated bubble consists on the insertion of a secondary vortices mechanism in the flow. This vortices mechanism of the control explains the variation of the boundary layer thickness previously observed.

The instability introduced by the actuator affects the periphery of the average recirculation region located downstream the rear end base and changes the overall shape of the top tori structure Fig. 18. The actuator effect on the wake region is not clearly observed, however modifications on velocity values are detected as well as a considerable raise of the separation

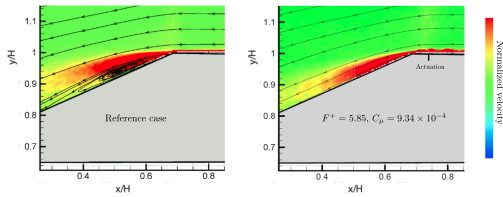


Fig. 17. Vorticity distribution. Reference case at the left, controlled flow (case1) at the right.

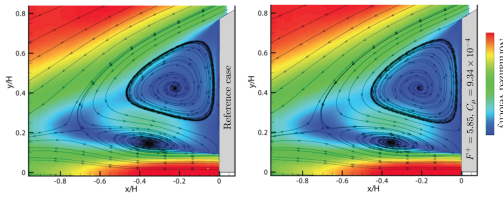


Fig. 18. Flow topology at the rear end base of the model. Reference case at the left, controlled flow (case1) at the right.

point.

4. CONCLUSIONS

This work highlights the physical behavior of the flow around Ahmed body geometry with 25° slant angle. The measured drag coefficients, for different Reynolds numbers, are in agreement with the literature. The in-house piezoelectric actuators are characterized, they are efficient for the separation flow control as they produce the required momentum and the suitable reduced frequencies for separation control. During the actuation at the top of the rear window, small swirling structures are developed, they move along the body and induce momentum at the close vicinity of the wall. So, the flow resists to the pressure gradient and it remains attached to the wall. For the studied Reynolds numbers, the maximum drag reduction obtained is about 10%. Through the present experimental study, we showed that the reduced frequency and the momentum coefficient are both parameters driving the control efficiency. However, the momentum coefficient seems not to be essential contrary to the reduced frequency that required more attention in order to fit with natural Kelvin-Helmholtz instability of the shear layer.

ACKNOWLEDGMENTS

The research work has been supported by Campus International pour la Sécurité et l'Intermodalité des Transports, la Région Nord-Pas-de-Calais, l'Union Européenne, la Direction de la Recherche, Enseignement Supérieur,

Santé et Technologies de l'Information et de la Communication et le Centre National de la Recherche Scientifique. The authors gratefully acknowledge the support of these institutions.

REFERENCES

- Ahmed, S. R., G. Ramm and G. Faltn (1984). Some salient features of the time-averaged ground vehicle wake, SAE Paper n°840300, Detroit, USA
- Aider, J. L., J. F. Beaudoin and J. E. Weisfreid (2010). Drag and lift reduction of a 3D bluff-body using active vortex generators. *Exp. Fluids* 48, 771-789.
- Aubrun, S., J. McNally, F. Alvi and A. Kourta (2011) Separation flow control on a generic ground vehicle using steady microjet arrays; *Exp. Fluids* 51, 1177-1187.
- Beaudoin, J. F. and J. L. Aider (2008). Drag and lift reduction of a 3D bluff body using flaps. *Exp. Fluids* 44(4), 491-501.
- Bruneau, C. H., P. Gilliéron and I. Mortazavi (2007). Flow manipulation around the Ahmed body with a rear window using passive strategies. *C. R. Mécanique* 335, 213-218.
- Bruneau, C. H. and I. Mortazavi (2008). Numerical modelling and passive flow control using porous media. *Comp. Fluids* 37(5), 488-498.
- Boucinha, V. (2009). *Etude de l'écoulement induit par une décharge à barrière diélectrique surfacique - Contribution au contrôle des écoulements subsoniques par actionneurs plasmas*. PhD Thesis, Orléans University.
- Chen, F. J., C. Yao, G. B. Beeler, R. Bryant and R. Fox (2000) Development of synthetic jet actuators for active flow control at NASA Langley. *AIAA Journal*. 2405-2413.
- Crittenden, T. M. and A. Glezer (2006) A high-speed, compressible synthetic jet. *Physics of Fluids* 8(1), 1-10.
- Duriez, T., J. Aider, J. E. Weisfreid and G. Artana (2011) Control of a massively separated flow through vortex pairing and phase locking; *International Journal of Heat and Fluid Flow* 1-4.
- Erk, P. P., *Separation control on a post-stall airfoil using acoustically gener-*

- ated perturbations.* PhD Thesis, Berlin University.
- Fourrié, G., L. Keirsbulck, L. Labraga and P. Gilliéron (2011). Bluff-body drag reduction using a deflector. *Exp. Fluids* 50(2), 385-395.
- Gilliéron, P. and A. Kourta (2010). Aerodynamic drag reduction by vertical splitter plates. *Exp. Fluids* 48(1), 1-16.
- Gilliéron, P. and A. Kourta (2013) Aerodynamic drag control by pulsed jets on simplified car geometry. *Exp. Fluids* 54, 1442-1454.
- Hinterberger, C., M. G. Villabla and W. Rodi (2003). Large eddy simulation of flow around the Ahmed body. In *The Aerodynamics of Heavy Vehicles: Trucks, Buses and Trains. Lecture Notes in Applied and Computational Mechanics* 20, 77-89.
- Ho, C. and L. S. Huang (1982) Subharmonics and Vortex Merging in Mixing Layers. *J. Fluid Mech.* 119, 443-473.
- Jenkins, L., S. A. Gorton and S. Anders (2002) Flow control device evaluation for an internal flow with an adverse pressure gradient. *AIAA Journal.* 226-235.
- Joseph, P., X. Amandolse and J. L. Aider (2011). Drag reduction on the 25° slant angle Ahmed reference body using pulsed jets. *Exp. Fluids.* 52(5), 1169-1185.
- Joseph P., X. Amandolese, C. Edouard and J. L. Aider (2013) Flow control using MEMS pulsed micro-jets on the Ahmed body. *Exp. Fluids* 54, 1442-1454.
- Joseph, P. (2012) *Application du contrôle par jets pulsés à un corps non profilé.* PhD thesis, University of Pierre et Marie Curie-Paris.
- Kotapati, R. B. and R. Mittal (2005) Time-accurate three-dimensional simulations of synthetic jets in quiescent air. *AIAA Journal* 103-120.
- Kourta, A. and P. Gilliéron (2009). Impact of the Automotive Aerodynamic Control on the Economic Issues. *Journal of Applied Fluid Mechanics* 2(2), 69-75.
- Krajnovic, S. and Davidson, L. (2005). Flow around a simplified car. *Journal of Fluids Engineering* 127, 907-928.
- Leclerc, C. (2008). *Réduction de la traînée d'un véhicule automobile simplifié à l'aide du contrôle actif par jet synthétique.* PhD thesis, University of Toulouse, France.
- Leclerc, C., E. Levallois, P. Gilliéron and A. Kourta (2006). Aerodynamic Drag Reduction by Synthetic Jet: A 2D Numerical Study Around a Simplified Car, *3rd AIAA- Flow Control Conference.* San Francisco, CA, USA.
- Leclerc, C., E. Levallois, Q. Gallas, P. Gilliéron and A. Kourta (2006) Phase locked analysis of a simplified car geometry wake flow control using synthetic jet. *Proceedings of FEDSM2006, FEDSM2006-98469 ASME Joint U.S. - European Fluids Engineering Summer Meeting, Miami, FL, July 17-20, 2006.*
- Lehugeur, B., P. Gilliéron and A. Kourta (2010) Experimental investigation on longitudinal vortex control over a dihedral bluff body. *Exp. Fluids* 48, 33-48.
- McCormick D. C. (2010) Boundary layer separation control with directed synthetic jets. *AIAA Journal* 519-531.
- Modi, V. J. (1997). Moving surface boundary-layer control: a review. *Journal of Fluids and Structures* 11(6), 627-663.
- Prasad, A. K., R. J. Adrian, C. C. Landreth and P. W. Offutt (1992) Effect of resolution on the speed and accuracy of particle image velocimetry interrogation. *Exp. Fluids* 13(2), 105-116.
- Pujals, G., S. Depardon and C. Cossu (2010). Drag reduction of a 3D bluff-body using coherent streamwise streaks. *Exp. Fluids* 49, 1085-1094.
- Rediniotis, O. K., J. Ko, X. Yue and A. J. Kurdila (1999) Synthetic jets, their reduced order modeling and applications to flow control. *AIAA Journal* 99-115.
- Rouméas, M., P. Gilliéron and A. Kourta (2005). Analyze and control of the near-wake flow over a simplified car geometry; *Proceedings of the 4th Symposium of Bluff Body Wake and Vortex-Induced Vibration (BBVIV4)*, Santorini Island.
- Rouméas, M., P. Gilliéron and A. Kourta (2006). Analyse and Control of the near-wake flow over square back geometry. *AIAA Paper*, San Francisco.

- Rouméas, M., P. Gilliéron and A. Kourta (2009) Analysis and control of the near-wake flow over a square-back geometry; *Computers & Fluids* 38, 60-70.
- Schaffler, N. W., T. E. Hepner, G. S. Jones and M. Kegerise (2002) Overview of active flow control actuator development at NASA Langley research center. *AIAA Journal* 3159-3167.
- Smith, B. L. and A. Glezer (2002) Jet vectoring using synthetic jets. *Journal of Fluid Mechanics* 458, 1-24.
- Smith, B. L. and G. W. Swift (2001) Synthetic jets at large Reynolds number and comparison to continuous jets. *AIAA Journal* 3030-3040.
- Tesar, V. and J. Kordik (2010) Time-mean structure of axisymmetric synthetic jets. *Sensors and actuators A*. 161, 217-224.
- Thacker, A. (2010). *Contribution expérimentale à l'analyse stationnaire et instationnaire de l'écoulement l'arrière d'un corps de faible allongement*. PhD thesis, Orléans University, France.
- Thacker, A., S. Aubrun, A. Leroy and P. Devinant (2010). Experimental characterization of the unsteady flow over the rear slant of a Ahmed body. *Proceedings of ASME 2010 3rd Joint US-European Fluids Engineering Summer Meeting & 8th International Conference on Nanochannels, Microchannels and Minichannels*.